# Exploring Mesoscopic Physics of Vacancy-Ordered Systems through Atomic Scale Observations of Topological Defects

A. Y. Borisevich,[1,*] A. N. Morozovska,[2,†] Young-Min Kim,[1,3] D. Leonard,[1] M. P. Oxley,[1,4] M. D. Biegalski,[1] E. A. Eliseev,[5] and S. V. Kalinin[1]

[1]*Oak Ridge National Laboratory, Oak Ridge, Tennessee 37831, USA*
[2]*Institute of Physics, National Academy of Sciences of Ukraine, 46, pr. Nauki, 03028 Kiev, Ukraine*
[3]*Korea Basic Science Institute, Daejeon 305-333, Korea*
[4]*Department of Physics and Astronomy, Vanderbilt University, Nashville, Tennessee 37240, USA*
[5]*Institute for Problems of Materials Science, National Academy of Sciences of Ukraine, 3, Krjijanovskogo, 03142 Kiev, Ukraine*

(Received 25 February 2012; published 10 August 2012)

Vacancy-ordered transition metal oxides have multiple similarities to classical ferroic systems including ferroelectrics and ferroelastics. The expansion coefficients for corresponding Ginzburg-Landau-type free energies are readily accessible from bulk phase diagrams. Here, we demonstrate that the *gradient* and *interfacial* terms can quantitatively be determined from the atomically resolved scanning transmission electron microscopy data of the topological defects and interfaces in model lanthanum-strontium cobaltite. With this knowledge, the interplay between ordering, chemical composition, and mechanical effects at domain walls, interfaces and structural defects can be analyzed.

DOI: 10.1103/PhysRevLett.109.065702 PACS numbers: 81.30.Bx

The properties and functionality of correlated oxides are intrinsically controlled by the oxygen stoichiometry that directly couples to the oxidation state of a transition metal, induces structural and metal-insulator transitions [1], and governs magnetic and transport properties [2]. A distinctive feature of nonstoichiometric oxides is the tendency for the formation of vacancy-ordered phases [3–7]. These ordering processes strongly affect electronic, transport, structural, ferroic, magnetic, and ionic properties of oxides, and hence are directly relevant for applications. For early *d* elements, the formation of oxygen vacancies at low nonstoichiometries is followed by the (irreversible) formation of crystallographic shear phases [8], directly involved in the functionality of the memristive and electroresistive electronics [9–11]. For mid- and late-3*d* elements, universal is the (reversible) ordering of the oxygen vacancy and formation of brownmillerite type structures [12,13]. This transition is induced by temperature and is associated with significant lowering of ionic conductivity and changes in magnetic properties due to cation transition from octahedral to tetrahedral coordination.

The transition from the disordered to the ordered phase induced by oxygen partial pressure, temperature, or other stimuli is an example of a symmetry lowering transition, analogous to ferroic (ferroelectric, ferromagnetic, ferroelastic) and antiferroic transformations. Oxygen vacancy order can thus be considered as an equivalent of a ferroic or antiferroic order parameter. In that case, we could expect vacancy-ordered compounds to support a variety of topological defects including antiphase and twin domain boundaries. In classical ferroics, the physical and ionic properties of these interfaces are different from the bulk and approach that of high-symmetry phase [14–18], and ferroic order is strongly affected by the presence of defects and interfaces [19–22]; similar phenomena can be expected to occur in vacancy-ordered oxides. The presence of moving boundaries combined with the difference in molar volumes and unit cell shape between ordered and disordered phase will lead to ferroelastic behavior, potentially including high strains and superplasticity [23]. Finally, the presence of several competing interactions (e.g., polarization and vacancy ordering or ferroelasticity and vacancy ordering) can give rise to morphotropiclike behavior.

These considerations necessitate the development of mesoscopic phase-field type models for the description of oxygen vacancy dynamics and ordering [7,24–29], similar to the Ginsburg-Landau-Devonshire (GLD) type theory for ferroelectrics that is now actively used for modeling ferroelectric phenomena in nonuniform systems [30–32]. Previously, phase-field models have been extensively used to model phase ordering phenomena [30]. However, while bulk free energy expansion terms can be readily obtained from thermodynamic phase diagrams [28], the gradient and interfacial terms that describe the structure and properties of topological defects, surfaces, and interfaces remain generally unknown.

Here, we demonstrate that structural information obtained by high-resolution (scanning) transmission electron microscopy (STEM) can be used to directly obtain these parameters, as well as to explore more subtle effects associated with domain wall behavior in the vicinity of surfaces and interfaces. While the imaging studies of vacancy ordering phenomena have been reported for several decades [33–35], recent advances in high-resolution imaging [36–40] make possible direct mapping of atomic structures and local strains on the atomic level, opening pathway to systematically probe the ferroic physics of vacancy-ordered systems.

 

As a model system, we have chosen the $(La_xSr_{1-x})CoO_3$ solid solutions. These materials are broadly explored as perspective cathodes for solid oxide fuel cells, driving significant effort at understanding ionic properties and formation of vacancy-ordered phases [41–43]. Furthermore, the link between oxygen nonstoichiometry and electronic properties is well studied [44]. Finally, formation of vacancy phases in these materials, albeit not the structure of topological defects, was repeatedly established [6,45].

Here we explore vacancy-ordered structures in $(La_{0.5}Sr_{0.5})CoO_{2.5}$ films grown on $NdGaO_3$ substrate by pulsed laser deposition. Micrographs were recorded using VG HB603U dedicated cold field emission gun STEM operated at 300 kV and equipped with Nion aberration corrector to give the probe size of ~0.7 Å. Shown in Fig. 1(a) is an example of the ordered phase in the LSCO, illustrating the presence of the antiphase boundary. Clear modulation of atomic spacings is observed inside LSCO, which is directly related to vacancy ordering in the brownmillerite structure (see e.g., Ref. [12]), where longer spacings correspond to oxygen-depleted CoO layers, and shorter spacings correspond to stoichiometric $CoO_2$ layers (see Supplementary Materials [46]). At the boundary, stoichiometric and depleted layers switch places, indicating a 1/2 u.c. shift of the vacancy-ordered supercell. To quantify the phase ordering phenomena, we use an approach originally developed for TEM image analysis of ferroelectric materials [36,47] and subsequently adapted for STEM [21,39,40]. Here, the atomic positions are determined with subpixel 3–10 pm precision (using NGO atomic spacings as an internal calibration standard) by direct fit of atomic column intensities and interatomic spacings can then be visualized, as shown in Fig. 1(b).

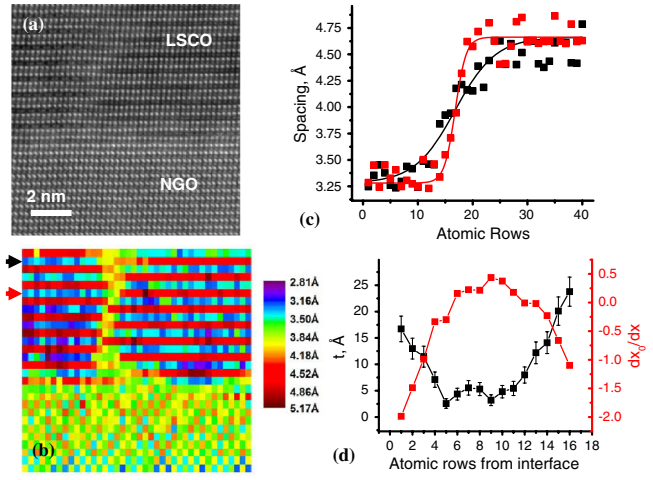


FIG. 1 (color online). (a) STEM image (low pass-filtered) of antiphase boundary in vacancy-ordered LSCO and (b) atomic spacing map. (c) two examples of the fit of the antiphase boundary profiles in each row (squares: experimental points, lines: tanh fits); the corresponding lines on the map in Fig. 1(b) are highlighted by the arrows of a matching color and (d) variation of the domain wall width (black) and derivative of the wall position (red; related to the wall angle) vs the distance from interface.

To describe the phase ordering process and the behavior of lattice parameters in the vicinity of the defects, we extend the phase-field approach suggested by Khachaturyan (Ref. [48]) and introduce the free energy density in the parent cubic phase as:

$$f = \frac{\alpha}{2}c^2\eta^2 + c\frac{k_BT}{2}S(\eta) + \frac{g}{2}c(\nabla\eta)^2 - \frac{1}{2}s_{ijkl}\sigma_{ij}\sigma_{kl} + u_{kl}\sigma_{kl} - w(\eta, \sigma_{ij}). \quad (1)$$

Here the first term governs interaction between vacancies, favoring the ordering of vacancies for $\alpha < 0$. $S(\eta) = ((1-\eta)\ln(1-\eta) + (1+\eta)\ln(1+\eta))$ is the configurational entropy of the system with the concentration of vacancies $c$. The order parameter, $\eta$, defines the relative occupation numbers for the sublattices (two sets of alternating planes), $\delta n_a = c(1-\eta)/(2N_a)$ and $\delta n_b = c(1+\eta)/(2N_a)$), so that the total occupation is constant, $\delta n_a + \delta n_b = c/N_a$, $N_a$ is the stoichiometric concentration of oxygen. Values $\eta = \pm 1$ correspond to the complete ordering of vacancies in either sublattice "$b$" or "$a$", while $\eta = 0$ corresponds to the complete disorder (with equal occupation of the two sublattices). Coupling constant $\alpha < 0$ and the gradient coefficient $g > 0$; i.e., the vacancies tend to order and the corresponding boundaries have positive correlation energy. $\sigma_{ij}$ is the stress, $s_{ijkl}$ is elastic compliances tensor, and $u_{ij}$ is tensor of elastic strains. The term $u_{kl}\sigma_{kl}$ originates from the Legendre transformation required to account for mechanical boundary conditions.

The coupling between the order parameter $\eta$ and the stresses $\sigma_{ij}$ is defined by $w(\eta, \sigma_{ij})$ that can be represented as series in order parameter

$$w(\eta, \sigma_{ij}) = \beta_{ij}\sigma_{ij}c + B_{ij}\sigma_{ij}c^2\eta^2. \quad (2)$$

The first term in Eq. (2) is the chemical expansion of the lattice due to the appearance of vacancies ($\beta_{ij}$ is the elastic dipole tensor), the second one is chemical striction due to the ordering of vacancies [49]. Note that the term linear in $\eta$ is zero, as follows from translation symmetry of the sublattices.

Symmetry of the striction tensor $B_{ij}$ is determined by the local symmetry of the vacancy site, which could be different from the global symmetry of the media [50]. Here, we assume the tetragonal symmetry of $B_{ij}$, with tetragonal axis along $z$ axis. Finally, we note that free energy of the system is $F = \int_0^h f dz + \frac{\lambda}{2}(\eta^2(0) + \eta^2(h))$, where the last term $\frac{\lambda}{2}(\eta^2(0) + \eta^2(h))$ is the contribution of surface or interface energy. $\lambda$ is extrapolation length,. whose geometrical sense is described in, e.g., Ref. [51]. The length depends on the surface/interface state and is poorly known for ferroics and can be estimated as 1–100 nm [36].

The free energy Eq. (1) can be used to analyze the ground state of the system, as well as the structure of topological defects and interfaces. The structure of thin film on rigid substrate is defined by tetragonality $t = (c-a)/a = (u_{33} - u_{11})/(1 + u_{11})$ that can be found as

$$t \approx \frac{s_{12} - s_{11}}{s_{11} + s_{12}} u_m + \left(B_{33} - \frac{2 s_{12} B_{11}}{s_{11} + s_{12}}\right) c^2 \eta^2. \quad (3)$$

Film-substrate misfit strain is $u_m$. In comparison, in a freestanding films $t \approx (B_{33} - B_{11}) c^2 \eta^2$.

For the case of antiphase domain boundary (APB) in the bulk, the strain and stress distributions are nonzero and the order parameter profile along $x$ axis can be derived as

$$\eta_{\text{bulk}}(x) = \eta_b \tanh\left(\frac{x - x_0}{L_C^b}\right). \quad (4)$$

Where $\eta_b \approx \sqrt{-3(\alpha c + k_B T)/k_B T}$ is bulk (equilibrium) value of order parameter, $x$ is a coordinate, $x_0$ is the position of APB, and $L_C^b$ is bulk correlation length. The analytical expressions for stress and strain components are given in the Supplementary Materials [46].

The order parameter in the single-domain regions of LSCO becomes $z$ dependent in the vicinity of the NGO interface. The dependence can be obtained from the solution of 1D problem with boundary conditions $\eta(z = 0) - \lambda \partial(\eta(z = 0))/\partial z = 0$ and $\sigma_{i3}(z = 0) = 0$; it is:

$$\eta_{\text{SD}}(z) \approx \eta_b \left(1 - \frac{1}{1 + \sqrt{2}\lambda / L_C(0)} \exp\left(-\frac{\sqrt{2} z}{L_C(0)}\right)\right) \quad (5)$$

Where the amplitude $\eta_{\text{SD}}(z)$ becomes close to the bulk value $\eta_b$ at distances $z > L_C^b$; $z$-dependent wall width $L_C(z)$ is insensitive to the boundary condition and approximate expression is valid $\frac{1}{L_C(z)} \approx \sqrt{\frac{\alpha c + k_B T - 2 B_{ij} \sigma_{ij}(0,z)}{-2g}}$ (see Suppl. Mat.)

Then the order parameter of domain wall approaching the interface can be analyzed using the perturbation method [52]. In this case, the 2D problem is solved with the boundary conditions $\eta(x, 0) - \lambda \partial(\eta(x, 0))/\partial z = 0$ and $\sigma_{i3}(x, 0) = 0$. The APB profile is then

$$\eta(x, z) \approx \eta_{\text{SD}}(z) \tanh\left(\frac{x - x_0}{L_C(z)}\right) \quad (6)$$

As anticipated Eq. (6) at $|x - x_0| \gg 10 L_C$ it transforms into Eq. (5), $\eta(x, z) \to \pm \eta_{\text{SD}}(z)$, and thus describes the order parameter $z$ behavior far from the APB.

These behaviors are illustrated in Fig. 2(a) that shows the contour map of the order parameter $\eta(x, z)$ calculated in the vicinity of the APB-surface junction. Figs. 2(b) shows the contour map of the vacancy concentrations $\delta n_a(x, z)$ and $\delta n_b(x, z)$ calculated in the vicinity of the junction. It is seen from the Figs. 2(a) and 2(b) that APB broadens approaching the junction. The broadening region of about 10 lattice constants originates from elastic stress contribution $2 B_{ij} \sigma_{ij}(0, z)$ into $L_C(z)$. Corresponding contour maps for the strain fields $u_{11}(x, z)$ and $u_{33}(x, z)$ are shown in Figs. 2(c) and 2(d). Strains are minimal at the APB-surface junction. $u_{11}(x, z)$ adopt constant minimal value at the wall plane, and increases and saturates far from the wall. $u_{33}(x, z)$ tends to the constant bulk value $u_{33}^{\text{bulk}}$ far from the junction.

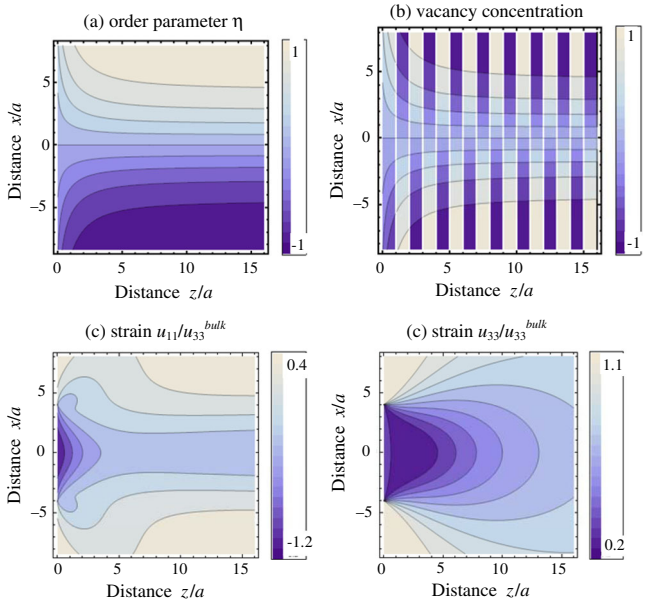


FIG. 2 (color online). (a) Contour map of the order parameter $\eta(x, z)$ calculated in the vicinity of the APB-surface junction. (b) Contour map of the layer-averaged vacancy concentration ($\delta n_a(x, z)$ for "even" planes 0, 2, 4, etc., and $\delta n_b(x, z)$ for "odd planes 1, 3, 5, etc.) calculated in the vicinity of the APB-surface junction. Strain field $u_{11}(x, z)/u_{33}^{\text{bulk}}$ (c) and $u_{33}(x, z)/u_{33}^{\text{bulk}}$ (d) calculated for natural boundary condition $\partial(\eta(x, 0))/\partial z = 0$ and elastically free interface $\sigma_{i3}(x, 0) = 0$. Parameters $L_C^b = 4a$, $B_{11}/B_{33} = 0.4$; lattice constant is $a$. Color bars to each plot indicate the corresponding value of the $\eta(x, z)$ and strains, which are dimensionless.

Figure 3(a) shows profiles of the order parameter $\eta$ and strain fields far away from the interface $z = 0$. It is seen that $\eta$ profile is tanh-like, $u_{33}$ is constant, $u_{11}$ has a dip at the APB. Approaching the interface $z = 0$, $\eta$ and $u_{33}(x, z)$ strongly depend on extrapolation length $\lambda$ as demonstrated in Figs. 3(b) and 3(c). The smaller $\lambda$ is, the wider the interface region where $\eta$ and $u_{33}$ changes, i.e., the stronger their gradient. Surface values $u_{33}(z = 0)/u_{33}^{\text{bulk}}$ and $\eta(z = 0)/\eta_b$ depends on the extrapolation length $\lambda$ far away from the APB as shown in Fig. 3(d). The surface values monotonically increase and saturate as $\lambda$ increases.

This derivation allows analyzing the structure of the antiphase boundary in Fig. 1. Here, we estimate the local width of the boundary by fitting the profile to the functional form of Eq. (5). Two examples of the fits with different $t$ values are given in Fig. 1(c); experimental data behavior is well described by the fitting function. Figure 1(d) shows the dependence of the fit parameter $t$ on the distance from the interface; the dependence is nonmonotonic. However, when compared with the plot of $dx_0/dx$ (proportional to tangent of the wall angle with respect to a normal to interface, such that $dx_0/dx = 0$ when the wall is oriented along the said normal), it is clear that the width is the smallest when the wall is vertical and

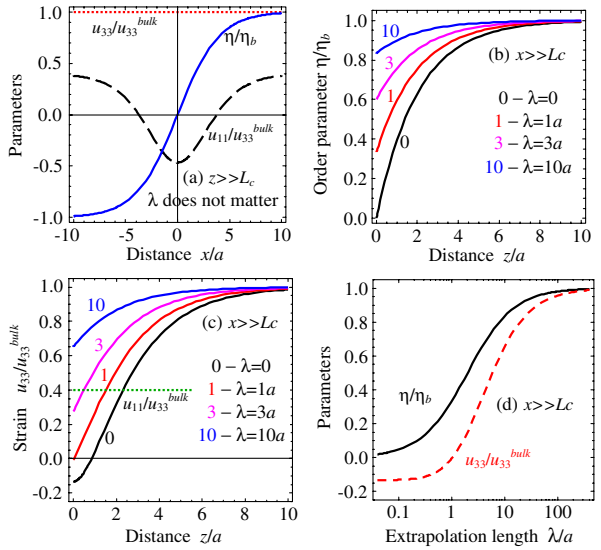


FIG. 3 (color online). (a) APB-profiles of the order parameter $\eta/\eta_b$ and strain field $u_{11}(x,z)/u_{33}^{\text{bulk}}$ and $u_{33}(x,z)/u_{33}^{\text{bulk}}$ calculated far away from the interface $z=0$ (i.e., $z \gg L_C^b$). Order parameter $\eta/\eta_b$ (b) and strain field $u_{33}(x,z)/u_{33}^{\text{bulk}}$ (c) approaching the interface $z=0$ calculated far away from the APB (i.e. $x \gg L_C^b$) for different extrapolation length $\lambda = 0$, 1, 3, 10 lattice constants $a$. (d) Surface values $u_{33}(z=0)/u_{33}^{\text{bulk}}$ and $\eta(z=0)/\eta_b$ vs extrapolation length $\lambda$ calculated far away from the APB (i.e., $x \gg L_C^b$).

increases steeply as the orientation deviates from 90 degrees.

Similar approach can be extended to analyze the ordering behavior at the interfaces. Figure 4(a) shows a typical HAADF image of a near interface region of a LSCO/NGO film. Figure 4(b) shows the dependence of the lattice parameter (averaged over 10 images of LSCO/NGO interface) on the distance $z$ from the interface. To fit the data, spacing profiles calculated for individual images were approximated with an exponential decay function; average of the fits of all profiles is shown as a black line. The local difference between the spacings of the stoichiometric and depleted layers is a measure of the degree of vacancy order. Comparison of the experimental Electron Energy Loss spectra (EELS) profiles to theoretical simulations suggest that experimentally observed profile widths are very close to the simulated ones. While partial cation intermixing cannot be completely excluded, it should be limited to the one layer immediately at the interface (See Supplementary Materials Fig. S2, [46]). Thus the value of $L_C$ obtained can be viewed as a (close) upper estimate.

In accordance with Eq. (5) approximate expression for the order parameter distribution in the near-surface gradient region is $\eta(z) \approx \eta_b(1 - \frac{1}{1+\sqrt{2}\lambda/L_C}\exp(-\frac{\sqrt{2}z}{L_C}))$. From the average of the corresponding exponential decay fits, $\eta(z) = 0.787(1 - 0.5\exp(-\frac{z-1}{1.1}))$, we extracted the fitting parameters: $L_C = 1.6$ lattice constants,

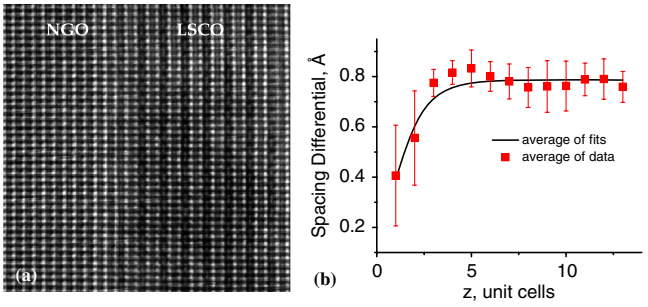


FIG. 4 (color online). (a) HAADF image of the NGO/LSCO interface showing rapid onset of cation order; (b) profile of a spacing differential of depleted vs stoichiometric planes as a function of the distance from the interface: red squares—experimental profile averaged over 10 images, black line—average of the corresponding exponential decay fits (see text).

$\eta_b = 0.8$ angstroms and $\langle\lambda\rangle = 1.1$ lattice constants (only average is determined since $\lambda$ may vary between dissimilar locations). Estimating LSCO ordering temperature as $T_O = 1000$ K and $\alpha c = -k_B T_O$, and using $L_C \approx \sqrt{-2g/(\alpha c + k_B T)} = 1.6$ lattice constants, $T = 300$ K ($k_B = 1.3807 \times 10^{-23}$ J/K), we can estimate the gradient coefficient $g$ in Eq. (1) as $g = 1.9 \times 10^{-39}$ J m$^2$. This constitutes first direct measurement of the $d$ interfacial terms controlling topological defects and interface structure in vacancy-ordered oxides. Notably, the gradient energy density $gc \sim 10^{-12}$ J/m in chemically ordered system is comparable to that in ferroelectrics, $\gamma P_S^2 \sim 10^{-12}$ J/m, and in ferroelastics, $\upsilon\Phi_S^2 \sim 10^{-12}$ J/m [15,53,54].

To summarize, high-resolution scanning transmission electron microscopy data is used to analyze the structure of the antiphase boundary (APB), APB-interface junction, and interfaces is vacancy-ordered LSCO. The numerical analysis of the atomic displacement profiles allows corresponding gradient and interfacial terms in free energy expansion to be derived. This in turn provides information for phase-field modeling of the vacancy ordering phenomena and phase separation in inhomogeneous systems under chemical, mechanical, and electrical stimuli, and is likely to have broad applicability for modeling of solid oxide fuel cell and memristive materials, as well as understanding basic physics of these materials. The proposed approach is universal and can be applied to other vacancy-ordered systems.

This work was supported (A. B., YM. K., D. L., S. V. K.) by the U.S. Department of Energy, Basic Energy Sciences, Materials Sciences and Engineering Division. E. A. E. and A. N. M. are thankful to National Academy of Sciences of Ukraine for support. A portion of this research (MB) was conducted at the Center for Nanophase Materials Sciences, which is sponsored at Oak Ridge National Laboratory by the Scientific User Facilities Division, Office of Basic Energy Sciences, U.S. Department of Energy.

*Corresponding author.
albinab@ornl.gov
†Corresponding author.
morozo@voliacable.com

[1] J. F. Mitchell, D. N. Argyriou, C. D. Potter, D. G. Hinks, J. D. Jorgensen, and S. D. Bader, Phys. Rev. B **54**, 6172 (1996).
[2] M. Imada, A. Fujimori, and Y. Tokura, Rev. Mod. Phys. **70**, 1039 (1998).
[3] K. Q. Huang, R. S. Tichy, and J. B. Goodenough, J. Am. Ceram. Soc. **81**, 2565 (1998).
[4] H. Kruidhof, H. J. M. Bouwmeester, R. H. E. Vondoorn, and A. J. Burggraaf, Solid State Ionics **63–65**, 816 (1993).
[5] J. F. Scott and M. Dawber, Appl. Phys. Lett. **76**, 3801 (2000).
[6] R. F. Klie, Y. Ito, S. Stemmer, and N. S. Browning, Ultramicroscopy **86**, 289 (2001).
[7] S. Semenovskaya and A. G. Khachaturyan, Phys. Rev. Lett. **67**, 2223 (1991).
[8] K. Szot, M. Rogala, W. Speier, Z. Klusek, A. Besmehn, and R. Waser, Nanotechnology **22**, 254001 (2011).
[9] D. H. Kwon, K. M. Kim, J. H. Jang, J. M. Jeon, M. H. Lee, G. H. Kim, X. S. Li, G. S. Park, B. Lee, S. Han, M. Kim, and C. S. Hwang, Nature Nanotech. **5**, 148 (2010).
[10] R. Waser, R. Dittmann, G. Staikov, and K. Szot, Adv. Mater. **21**, 2632 (2009).
[11] A. Sawa, Mater. Today **11**, 28 (2008).
[12] T. G. Parsons, H. D'Hondt, J. Hadermann, and M. A. Hayward, Chem. Mater. **21**, 5527 (2009).
[13] E. V. Tsipis and V. V. Kharton, J. Solid State Electrochem. **15**, 1007 (2011).
[14] J. Seidel, L. W. Martin, Q. He, Q. Zhan, Y. H. Chu, A. Rother, M. E. Hawkridge, P. Maksymovych, P. Yu, M. Gajek, N. Balke, S. V. Kalinin, S. Gemming, F. Wang, G. Catalan, J. F. Scott, N. A. Spaldin, J. Orenstein, and R. Ramesh, Nature Mater. **8**, 229 (2009).
[15] A. K. Tagantsev, E. Courtens, and L. Arzel, Phys. Rev. B **64** (2001).
[16] E. Salje and H. L. Zhang, Phase Transit. **82**, 452 (2009).
[17] J. Salafranca, R. Yu, and E. Dagotto, Phys. Rev. B **81**, 245122 (2010).
[18] A. Tselev, V. Meunier, E. Strelcov, W. A. Shelton, I. A. Luk'yanchuk, K. Jones, R. Proksch, A. Kolmakov, and S. V. Kalinin, ACS Nano **4**, 4412 (2010).
[19] V. Nagarajan, I. B. Misirlioglu, C. L. Jia, H. Kohlstedt, R. Waser, S. P. Alpay, and R. Ramesh, Appl. Phys. Lett. **86**, 192910 (2005).
[20] C. L. Jia, S. B. Mi, K. Urban, I. Vrejoiu, M. Alexe, and D. Hesse, Phys. Rev. Lett. **102**, 117601 (2009).
[21] A. Y. Borisevich, H. J. Chang, M. Huijben, M. P. Oxley, S. Okamoto, M. K. Niranjan, J. D. Burton, E. Y. Tsymbal, Y. H. Chu, P. Yu, R. Ramesh, S. V. Kalinin, and S. J. Pennycook, Phys. Rev. Lett. **105**, 087204 (2010).
[22] H. J. Chang, S. V. Kalinin, A. N. Morozovska, M. Huijben, Y. H. Chu, P. Yu, R. Ramesh, E. A. Eliseev, G. S. Svechnikov, S. J. Pennycook, and A. Y. Borisevich, Adv. Mater. **23**, 2474 (2011).
[23] W. F. Rao, M. Wuttig, and A. G. Khachaturyan, Phys. Rev. Lett. **106**, 105703 (2011).
[24] L. Q. Chen and A. G. Khachaturyan, Scr. Metall. Mater. **25**, 61 (1991).
[25] A. G. Khachaturyan, S. V. Semenovskaya, and J. W. Morris, Phys. Rev. B **37**, 2243 (1988).
[26] D. N. Fan and L. Q. Chen, J. Am. Ceram. Soc. **78**, 1680 (1995).
[27] Y. Z. Wang, H. Y. Wang, L. Q. Chen, and A. G. Khachaturyan, J. Am. Ceram. Soc. **78**, 657 (1995).
[28] J. Katamura and T. Sakuma, Acta Mater. **46**, 1569 (1998).
[29] J. Katamura and T. Sakuma, J. Am. Ceram. Soc. **80**, 2685 (1997).
[30] L. Q. Chen, Annu. Rev. Mater. Res. **32**, 113 (2002).
[31] Y. L. Li, S. Y. Hu, Z. K. Liu, and L. Q. Chen, Appl. Phys. Lett. **78**, 3878 (2001).
[32] J. Slutsker, A. Artemev, and A. Roytburd, Phys. Rev. Lett. **100**, 087602 (2008).
[33] A. Camanzi, Philos. Mag. **21**, 649 (1970).
[34] G. Vantendeloo, H. W. Zandbergen, and S. Amelinckx, Solid State Commun. **63**, 603 (1987).
[35] C. L. Jia, B. Kabius, H. Soltner, U. Poppe, and K. Urban, Physica (Amsterdam) **172C**, 81 (1990).
[36] C. L. Jia, V. Nagarajan, J. Q. He, L. Houben, T. Zhao, R. Ramesh, K. Urban, and R. Waser, Nature Mater. **6**, 64 (2007).
[37] C. L. Jia, S. B. Mi, M. Faley, U. Poppe, J. Schubert, and K. Urban, Phys. Rev. B **79**, 081405 (2009).
[38] A. Borisevich, O. S. Ovchinnikov, H. J. Chang, M. P. Oxley, P. Yu, J. Seidel, E. A. Eliseev, A. N. Morozovska, R. Ramesh, S. J. Pennycook, and S. V. Kalinin, ACS Nano **4**, 6071 (2010).
[39] C. T. Nelson, B. Winchester, Y. Zhang, S. J. Kim, A. Melville, C. Adamo, C. M. Folkman, S. H. Baek, C. B. Eom, D. G. Schlom, L. Q. Chen, and X. Q. Pan, Nano Lett. **11**, 828 (2011).
[40] M. F. Chisholm, W. D. Luo, M. P. Oxley, S. T. Pantelides, and H. N. Lee, Phys. Rev. Lett. **105**, 197602 (2010).
[41] S. B. Adler, Chem. Rev. **104**, 4791 (2004).
[42] N. B. Ivanova, S. G. Ovchinnikov, M. M. Korshunov, I. M. Eremin, and N. V. Kazak, Phys. Usp. **52**, 789 (2009).
[43] A. N. Petrov, V. A. Cherepanov, and A. Y. Zuev, J. Solid State Electrochem. **10**, 517 (2006).
[44] M. H. R. Lankhorst, H. J. M. Bouwmeester, and H. Verweij, Phys. Rev. Lett. **77**, 2989 (1996).
[45] J. Tao, D. Niebieskikwiat, M. Varela, W. Luo, M. A. Schofield, Y. Zhu, M. B. Salamon, J. M. Zuo, S. T. Pantelides, and S. J. Pennycook, Phys. Rev. Lett. **103**, 097202 (2009).
[46] See Supplementary Materials at http://link.aps.org/supplemental/10.1103/PhysRevLett.109.065702 for details of HAADF STEM studies and theoretical calculations.
[47] C. L. Jia, S. B. Mi, K. Urban, I. Vrejoiu, M. Alexe, and D. Hesse, Nature Mater. **7**, 57 (2008).
[48] A. G. Khachaturyan, *Theory of Structural Transformations in Solids* (Wiley, New York, 1983).
[49] A. P. Levanyuk, S. A. Minyukov, and A. Cano, Phys. Rev. B **66**, 014111 (2002).
[50] D. A. Freedman, D. Roundy, and T. A. Arias, Phys. Rev. B **80**, 064108 (2009).
[51] R. Kretschmer and K. Binder, Phys. Rev. B **20**, 1065 (1979).
[52] E. A. Eliseev, A. N. Morozovska, S. V. Kalinin, Y. L. Li, J. Shen, M. D. Glinchuk, L. Q. Chen, and V. Gopalan, J. Appl. Phys. **106**, 084102 (2009).
[53] J. Hlinka and P. Marton, Phys. Rev. B **74**, 104104 (2006).
[54] W. W. Cao and G. R. Barsch, Phys. Rev. B **41**, 4334 (1990).